Oxygen vacancies confined in hierarchically porous $CsPbBr_3$@Pb-MOF through in situ structural transformation for promoted photocatalytic CO_2 reduction

Yangwen Hou[a], Man Dong[c], Jingting He[a], Jing Sun[b], Chunyi Sun[c,*], Xiao Li[b], Xinlong Wang[c], Zhongmin Su[b,d,*]

[a]School of Materials Science and Engineering, Changchun University of Science and Technology, Changchun 130022, China

[b]Jilin Provincial Science and Technology Innovation Center of Optical Materials and Chemistry, School of Chemistry and Environmental Engineering, Changchun University of Science and Technology Changchun, Changchun, 130022 Jilin, China

[c]Key Laboratory of Polyoxometalate Science of Ministry of Education, Northeast Normal University, Changchun, 130024 Jilin, China

[d]State Key Laboratory of Supramolecular Structure and Materials, Institute of Theoretical Chemistry, College of Chemistry, Jilin University, Changchun 130021, China

* Corresponding author.

E-mail addresses: suncy009@nenu.edu.cn (C. Sun), zmsu@nenu.edu.cn (Z. Su).

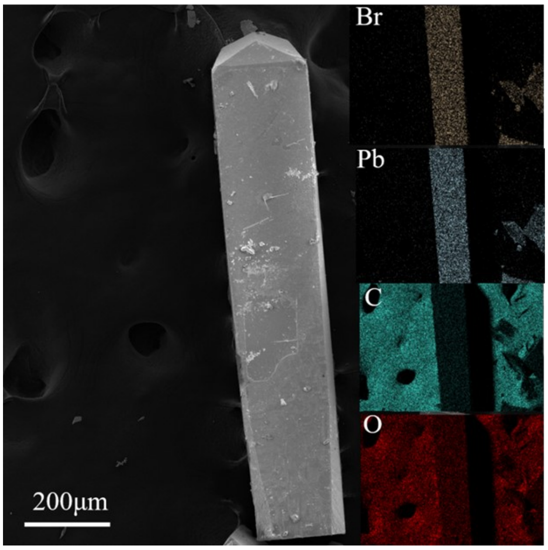

Fig.S1. SEM image and EDX mapping of PbBr-MOF

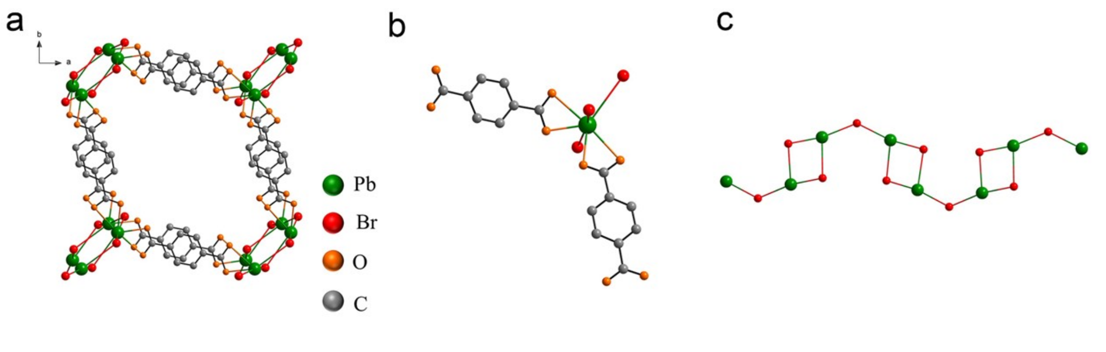

Fig. S2. Crystallographic view of (a) a single net of PbBr-MOF, (b) Coordination environment of the Pb(II) atom, (c) single $[Pb_2Br_3]^+$.

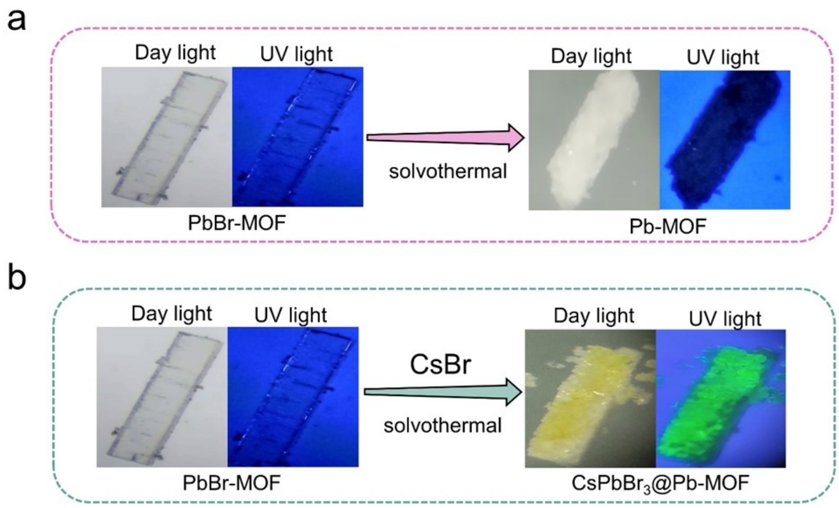

Fig. S3. Photographs of (a) PbBr-MOF and Pb-MOF, (b) PbBr-MOF and $CsPbBr_3$@Pb-MOF under daylight and UV light (365 nm).

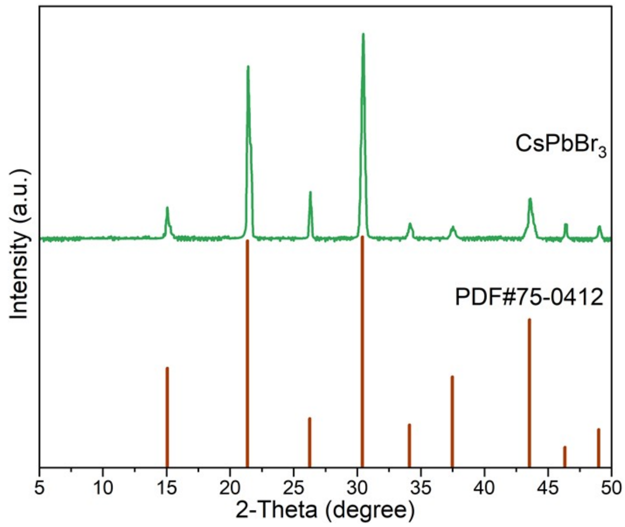

Fig. S4. PXRD pattern of $CsPbBr_3$.

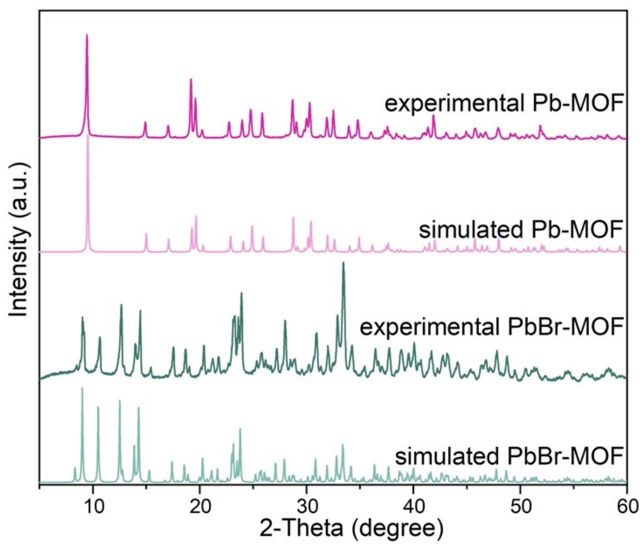

Fig. S5. PXRD pattern of PbBr-MOF and Pb-MOF.

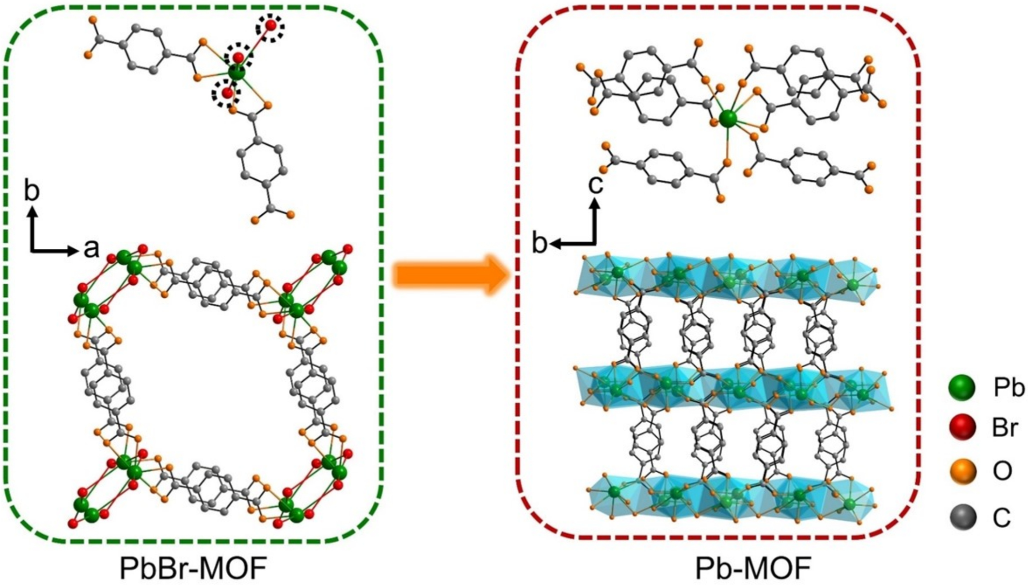

Fig. S6. Crystal structure of PbBr-MOF (left) and Pb-MOF (right)

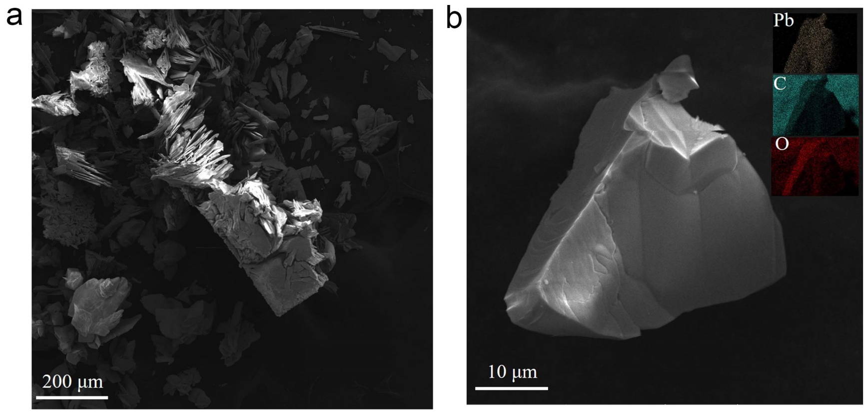

Fig. S7. SEM image and EDX mapping of Pb-MOF.

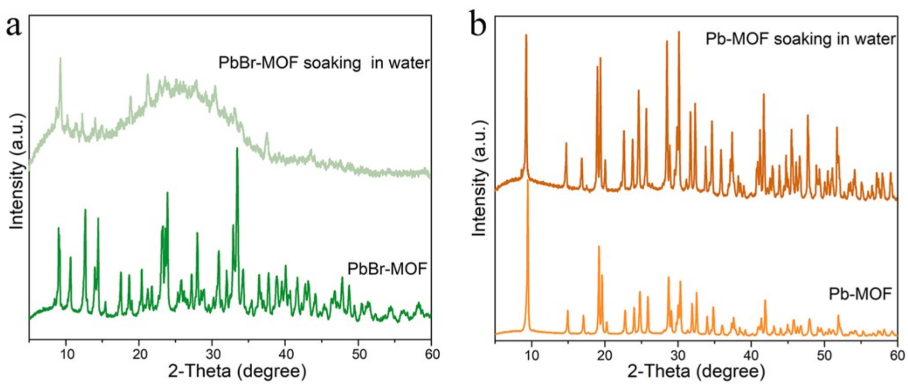

Fig. S8. PXRD patterns of (a)PbBr-MOF and (b) Pb-MOF after water immersion.

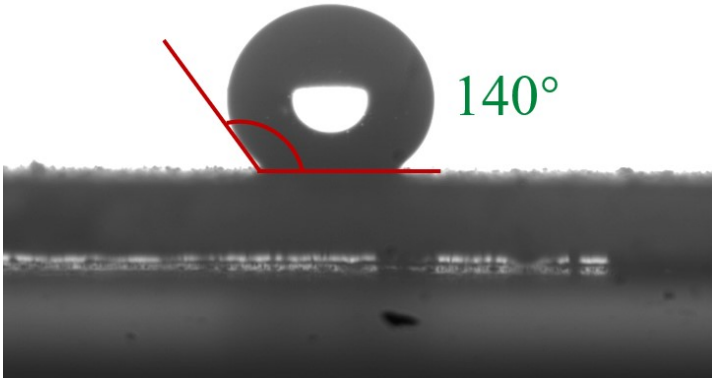

Fig. S9. Water contact angles of Pb-MOF.

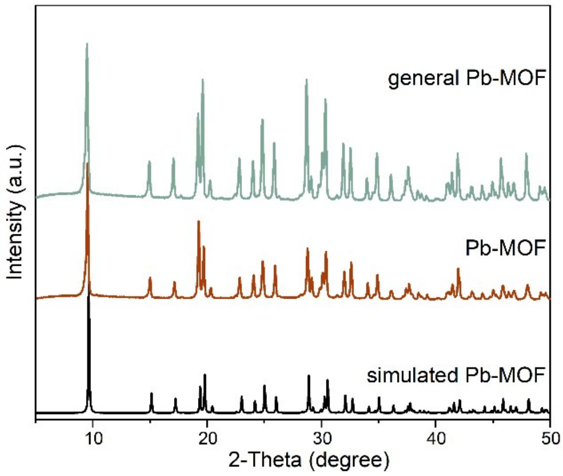

Fig. S10. PXRD pattern of Pb-MOF and general Pb-MOF.

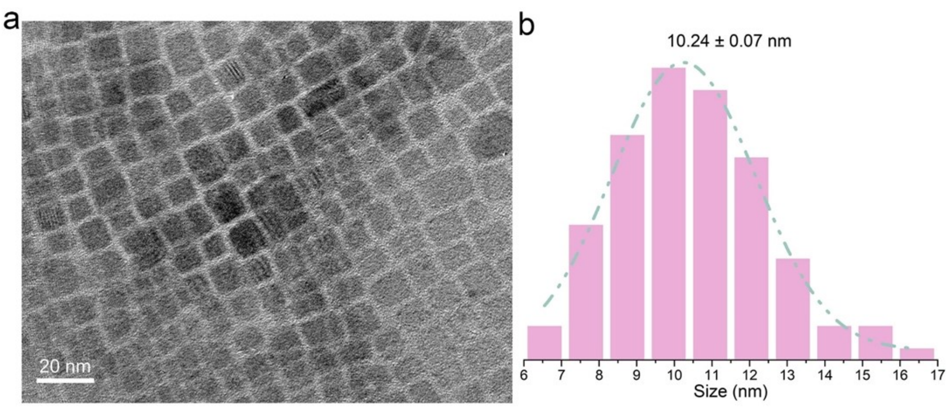

Fig. S11. (a) TEM image and particle size distributions of $CsPbBr_3$.

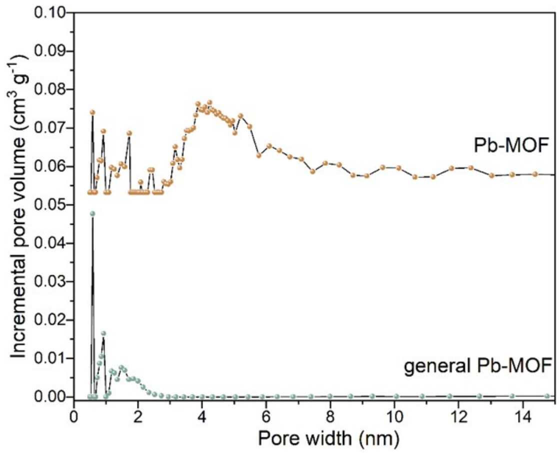

Fig. S12. Pore size distributions based on density-functional theory (DFT) analysis of Pb-MOF and general Pb-MOF.

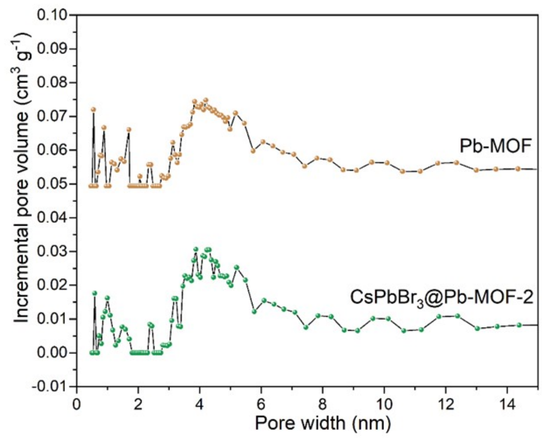

Fig. S13. Pore size distributions based on density-functional theory (DFT) analysis of Pb-MOF and $CsPbBr_3$@Pb-MOF-2.

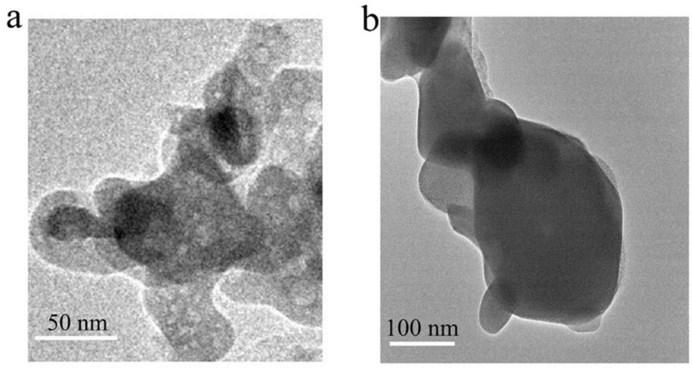

Fig. S14. TEM image of (a) Pb-MOF and (b) general Pb-MOF.

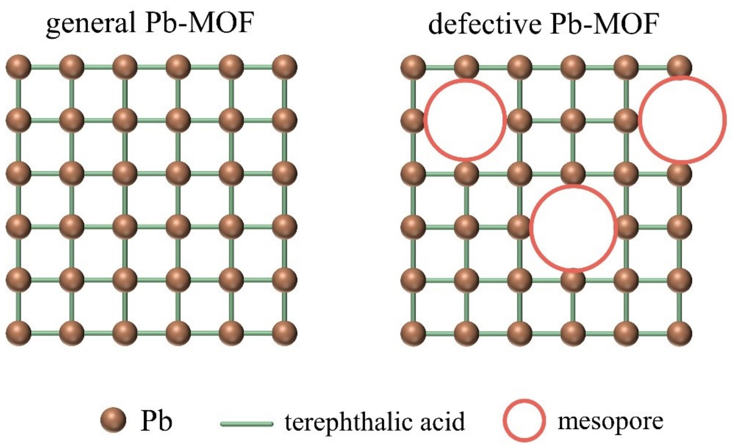

Fig. S15. Schematic showing the conversion of microporous MOFs into corresponding hierarchically porous structures based on the structural transformation.

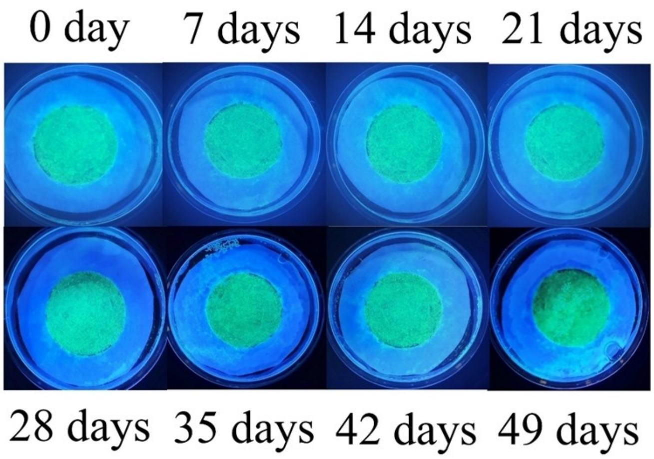

Fig. S16. Photographs of $CsPbBr_3$@Pb-MOF-2 in water under 365 nm UV light.

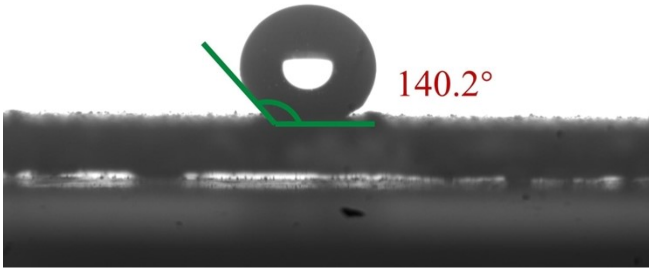

Fig. S17. Water contact angles of $CsPbBr_3$@Pb-MOF-2.

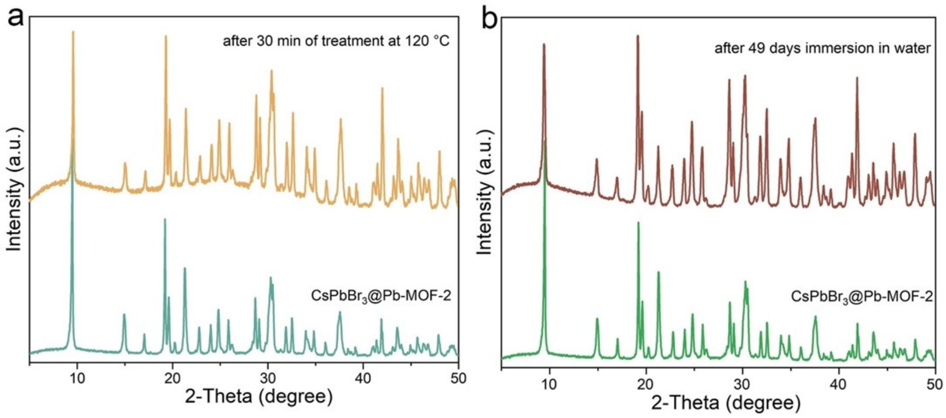

Fig. S18 PXRD pattern of $CsPbBr_3$@Pb-MOF-2 (a) after 49 days immersion in water and (b) after 30 min of treatment at 120 ℃.

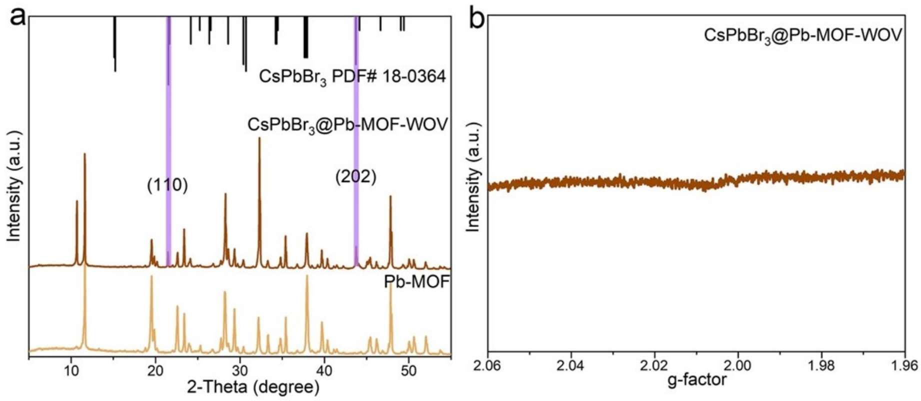

Fig. S19 (a) PXRD pattern of $CsPbBr_3$@Pb-MOF-WOV. (b) Electron paramagnetic resonance spectra of $CsPbBr_3$@Pb-MOF-WOV.

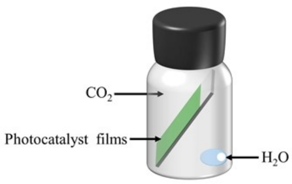

Fig. S20. Schematic of experimental set-up for photocatalytic CO_2 reduction with the assistance of H_2O.

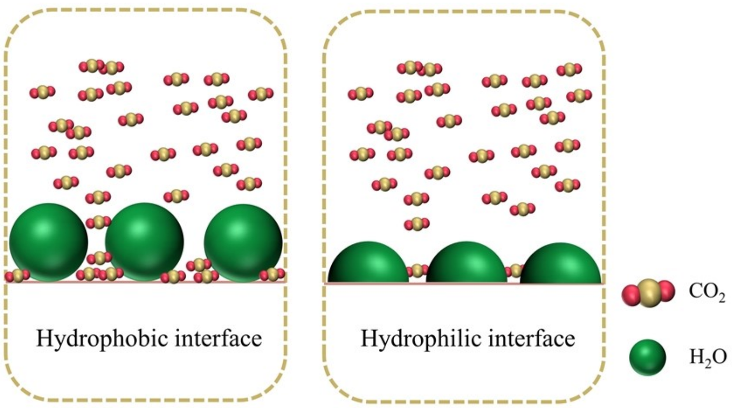

Fig. S21. The proposed photocatalytic reaction mechanism on the $CsPbBr_3$@Pb-MOF system for high selective.

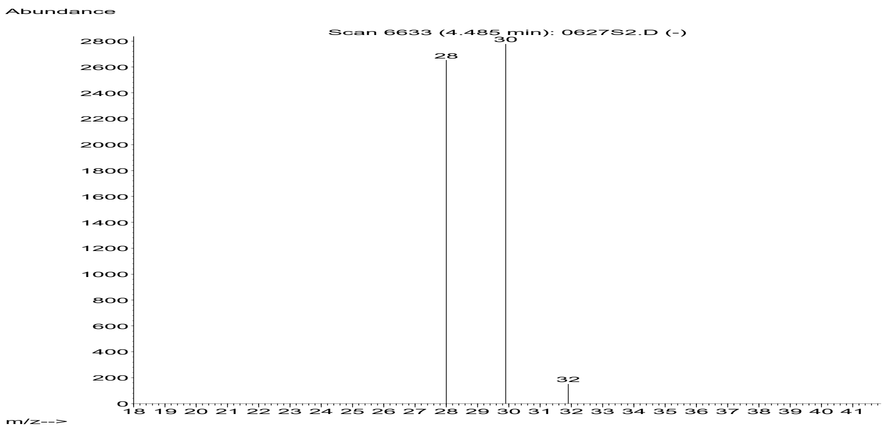

Fig.S22 Mass spectra of photocatalytic products generated in the atmosphere of CO_2 and $H_2{}^{18}O$ on $CsPbBr_3$@Pb-MOF.

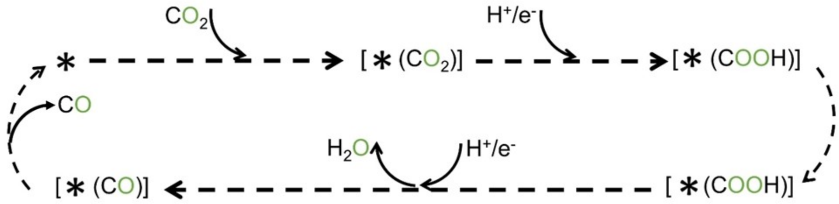

Fig.23 Schematic representation of the reduction of CO_2 to CO. where "*" represents the corresponding adsorption sites on the surface of the photocatalyst.

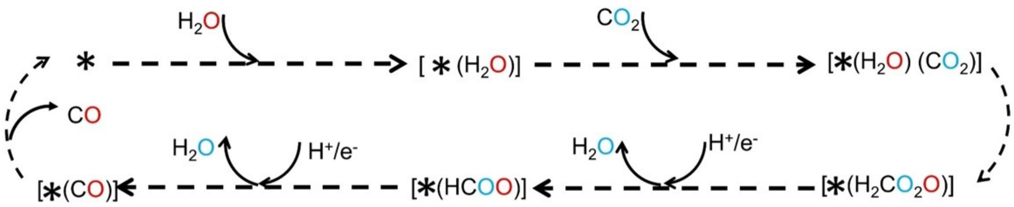

Fig.24 Schematic representation of the reduction of CO_2 to CO. where "*" represents the corresponding adsorption sites on the surface of the photocatalyst.

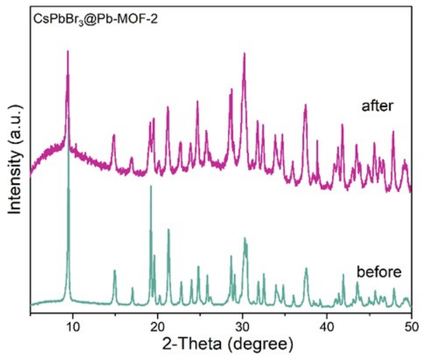

Fig. S25. PXRD pattern of $CsPbBr_3$@Pb-MOF-2 after 48h photocatalytic reduction CO_2 reaction cycles.

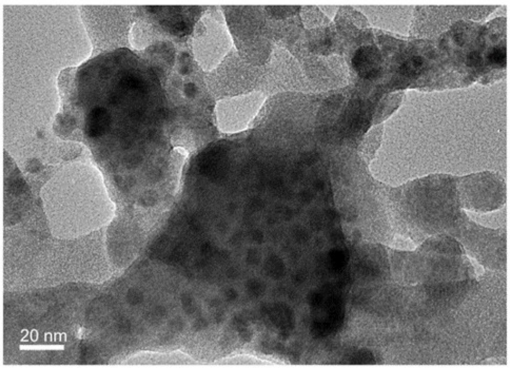

Fig. S26. TEM of $CsPbBr_3$@Pb-MOF-2 after 48h photocatalytic reduction CO_2 reaction cycles.

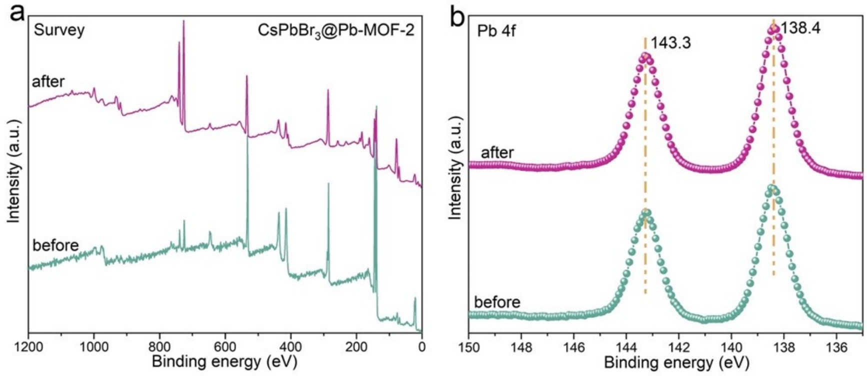

Fig. S27. XPS of $CsPbBr_3$@Pb-MOF-2 before and after 48h photocatalytic reduction CO_2 reaction cycles.

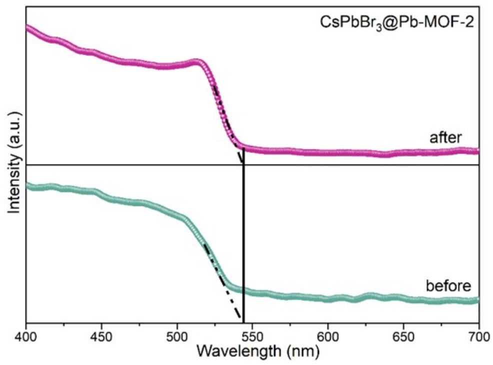

Fig. S28. UV-vis diffuse reflectance spectra of $CsPbBr_3$@Pb-MOF-2 before and after 48h photocatalytic reduction CO_2 reaction cycles.

Table S1. Time-resolved PL decay parameters of different samples under 365 nm excitation. The two-exponential decay curves were fitted using a non-linear least-squares method with a two-component decay law. The average lifetime (τ_{av}) was then determined using the equation:

Sample	τ_1(ns)	A_1	τ_2(ns)	A_2	X^2	τ_{av}(ns)
$CsPbBr_3$	19.50 (23.8%)	15.59	81.57 (76.2%)	11.95	1.089	66.8
$CsPbBr_3$@Pb-MOF-2	3.82 (53.9%)	356.1	22.16 (46.1%)	52.46	1.019	12.3

$$\tau = \sum_{i=1}^{i=n} A_i \tau_i^2 \Big/ \sum_{i=1}^{i=n} A_i \tau_i$$

Table S2. CO of selectivity of photocatalysts.

Photocatalyst	CO (μmol g^{-1})	H_2 (μmol g^{-1})	Selectivity(%)
$CsPbBr_3$@Pb-MOF-1	352.3	n.d.	100
$CsPbBr_3$@Pb-MOF-2	1284	10.1	99.2
$CsPbBr_3$@Pb-MOF-3	1066	8.7	99.2
$CsPbBr_3$@Pb-MOF-WOV	221	22.7	90
$CsPbBr_3$	149	20.3	88
Pb-MOF	n.d.	n.d.	

Reaction conditions: Photocatalyst (10 mg), reductant (H_2O, 100 μL), CO_2 (1 atm), λ> 420 nm, 12 hours reaction time; n.d. = Not detectable; Selectivety= (n (CO))/(n ($CO+H_2$))*100%, where n (CO) was the amount of CO (mol g^{-1}).

Table S3. Summary of perovskite-based photocatalysts for CO_2 reduction in gas-solid phase and liquid-solid phase.

Photocatalyst	Products (μmol g^{-1} h^{-1})	Reaction agent	Light source	Ref
$CsPbBr_3$@Pb-MOF	CO (107)	H_2O	300W Xe-lamp (λ>420 nm)	This work
$CsPbBr_3$@ZIF-8	CO (0.505) CH_4(1.811)	H_2O	100W Xe-lamp (AM, 1.5G)	1
$CsPbBr_3$@ZIF-67	CO (0.767) CH_4 (3.512)	H_2O	100W Xe-lamp (AM, 1.5G)	1
$CsPbBr_3$/MIL-100(Fe)	CO (20.4)	H_2O	300W Xe-lamp	2
$CsPbBr_3$NC/BZNW/MRGO	CO (0.58) CH_4 (6.29)	H_2O	150W Xe-lamp (λ>420 nm)	3
a-Fe_2O_3/AmineRGO/$CsPbBr_3$	CO (2.36) CH_4 (9.45)	H_2O	150W Xe-lamp (AM, 1.5G)	4
$CsPbBr_3$/Pd-NS	CO (1.92) CH_4 (3.47)	H_2O	150W Xe-lamp (λ>420 nm)	5
$CsPbBr_3$-Glycine	CO (27.7)	H_2O	300W Xe-lamp (λ>400 nm)	6
$CsPbBr_3$-GO-1.5	CH_4 (18.6)	H_2O	500W Xe-lamp (λ>400 nm)	7
Pb-rich Ni: $CsPbCl_3$	CO (169.37)	H_2O	300W Xe-lamp (AM, 1.5G)	8
$CsPbBr_3$ QDs@UiO-66 (NH_2)	CO (8.21) CH_4 (0.26)	H_2O /Ethyl acetate	300W Xe-lamp (λ>420 nm)	9
$MAPbI_3$@PCN-221(Fe0.2)	CO (4.16) CH_4 (13)	H_2O /Ethyl acetate	300W Xe-lamp (λ>400 nm)	10
$MAPbI_3$@PCN-221(Fe)	CO (14.16) CH_4 (6.24)	H_2O /Ethyl acetate	300W Xe-lamp (λ>400 nm)	10
MF/CPB-NWs	CO (81)	H_2O /Ethyl acetate	300W Xe-lamp (λ>420 nm)	11
$CsPbBr_3$/BIF-122-Co	CO (0.005) CH_4 (0.005)	H_2O /Ethyl acetate	300W Xe-lamp (λ>420 nm)	12
CPB@Cu-TCPP-20	CO (71.11) CH_4 (0.82)	Acetonitrile	300W Xe-lamp (λ>420 nm)	13
$CsPbBr_3$@g-C_3N_4-NH_2	CO (148.9)	H_2O /Ethyl acetate	300W Xe-lamp (λ>420 nm)	14

References

[1] Z.-C. Kong, J.-F. Liao, Y.-J. Dong, Y.-F. Xu, H.-Y. Chen, D.-B. Kuang, C.-Y. Su, Core@shell $CsPbBr_3$@Zeolitic imidazolate framework nanocomposite for efficient photocatalytic CO_2 reduction, *ACS Energy Lett.*, 2018, **3**, 2656–2662.

[2] R. Cheng, E. Debroye, J. Hofkens, M.B.J. Roeffaers, Efficient photocatalytic CO_2 reduction with MIL-100 (Fe)-$CsPbBr_3$ composites, *Catalysts*, 2020, **10**, 1352.

[3] Y. Jiang, J.-F. Liao, Y.-F. Xu, H.-Y. Chen, X.-D. Wang, D.-B. Kuang, Hierarchical $CsPbBr_3$ nanocrystal-decorated ZnO nanowire/macroporous graphene hybrids for enhancing charge separation and photocatalytic CO_2 reduction, J. Mater. Chem. A., 2019, **7**, 13762–13769.

[4] Y. Jiang, J.-F. Liao, H.-Y. Chen, H.-H. Zhang, J.-Y. Li, X.-D. Wang, D.-B. Kuang, All-solid-state Z-scheme α-Fe_2O_3/Amine-RGO/$CsPbBr_3$ hybrids for visible-light-driven photocatalytic CO_2 reduction, *Chem*, 2020, **6,** 766–780.

[5] Y.-F. Xu, M.-Z. Yang, H.-Y. Chen, J.-F. Liao, X.-D. Wang, D.-B. Kuang, Enhanced Solar-Driven Gaseous CO_2 Conversion by $CsPbBr_3$ Nanocrystal/Pd Nanosheet Schottky-Junction Photocatalyst, *ACS Appl. Energy Mater.*, 2018, **1**, 5083–5089.

[6] Y. Xu, W. Zhang, K. Su, Y.-X. Feng, Y.-F. Mu, M. Zhang, T.-B. Lu, Glycine-functionalized $CsPbBr_3$ nanocrystals for efficient visible-light photocatalysis of CO_2 reduction, *Chem. – Eur. J.*, 2021, **27**, 2305–2309.

[7] Y.-H. Chen, J.-K. Ye, Y.-J. Chang, T.-W. Liu, Y.-H. Chuang, W.-R. Liu, S.-H. Liu, Y.-C. Pu, Mechanisms behind photocatalytic CO_2 reduction by $CsPbBr_3$ perovskite-graphene-based nanoheterostructures, *Appl. Catal. B Environ.*, 2021, **284**, 119751.

[8] J. Zhu, Y. Zhu, J. Huang, L. Hou, J. Shen, C. Li, Synthesis of monodisperse water-stable surface Pb-rich $CsPbCl_3$ nanocrystals for efficient photocatalytic CO_2 reduction, *Nanoscale*, 2020,**12**,11842–11846.

[9] S. Wan, M. Ou, Q. Zhong, X. Wang, Perovskite-type $CsPbBr_3$ quantum dots/UiO-66(NH_2) nanojunction as efficient visible-light-driven photocatalyst for CO_2 reduction, *Chem. Eng. J.*, 2019, **358**,1287–1295.

[10] L.-Y. Wu, Y.-F. Mu, X.-X. Guo, W. Zhang, Z.-M. Zhang, M. Zhang, T.-B. Lu, Encapsulating Perovskite Quantum Dots in Iron-Based Metal–Organic Frameworks (MOFs) for Efficient Photocatalytic CO_2 Reduction, *Angew. Chem. Int. Ed.*, 2019, **58**, 9491–9495.

[11] Y. Xi, X. Zhang, Y. Shen, W. Dong, Z. Fan, K. Wang, S. Zhong, S. Bai, Aspect ratio dependent photocatalytic enhancement of $CsPbBr_3$ in CO_2 reduction with two-dimensional metal organic framework as a cocatalyst, *Appl. Catal. B Environ.*, 2021, **297**, 120411.

[12] Z.-Y. Chen, Q.-L. Hong, H.-X. Zhang, J. Zhang, Composite of $CsPbBr_3$ with Boron Imidazolate Frameworks as an Efficient Visible-Light Photocatalyst for CO_2 Reduction, *ACS Appl. Energy Mater.*, 2022, **5**, 1175–1182.

[13] N. Zhang, J.-J. Li, Y. Li, H. Wang, J.-Y. Zhang, Y. Liu, Y.-Z. Fang, Z. Liu, M. Zhou, Visible-light driven boosting electron-hole separation in $CsPbBr_3$ QDs@2D Cu-TCPP heterojunction and the efficient photoreduction of CO_2, *J. Colloid Interface Sci.*, 2022, **608**, 3192–3203.

[14] M. Ou, W. Tu, S. Yin, W. Xing, S. Wu, H. Wang, S. Wan, Q. Zhong, R. Xu, Amino-Assisted Anchoring of $CsPbBr_3$ Perovskite Quantum Dots on Porous g-C_3N_4 for Enhanced Photocatalytic CO_2 Reduction, *Angew. Chem*., 2018, **130**, 13758–13762.